CrystEngComm

ROYAL SOCIETY OF CHEMISTRY

COMMUNICATION

View Article Online
View Journal | View Issue

Cite this: *CrystEngComm*, 2022, **24**, 475

Received 20th October 2021,
Accepted 1st December 2021

DOI: 10.1039/d1ce01418h

rsc.li/crystengcomm

Stepwise synthesis of Zr-based metal–organic frameworks: incorporating a trinuclear zirconocene-based metallo-pyridine ligand†

Juan Zhu,[a] Zhao-Yang Liu,[a] Shuang-bao Li,*[b] He Huang,[a] Bao-Xu Jiang[a] and Yu-Teng Zhang *[a]

Two isostructural heterometallic ZrMOFs (denoted as ZrMOF-Co and ZrMOF-Ni) were obtained by a stepwise synthesis approach. Single-crystal X-ray structural analyses indicate that the two ZrMOFs are both built from trinuclear zirconocene-based metallo-pyridine building blocks, featuring a 2D infinite chain structure. Furthermore, magnetic studies reveal that ZrMOF-Co shows antiferromagnetic performance, while ZrMOF-Ni features a ferromagnetic behavior.

Metal–organic frameworks (MOFs), as a new class of outstanding porous crystalline materials, have been widely researched in gas storage separation, catalysis, magnetism, sensing and other fields.[1–4] The design and synthesis of various MOFs with new properties and functions are a major research focus. Among MOFs, zirconium-based metal–organic frameworks (ZrMOFs), owing to their abundant structure types, superior stability, fascinating properties and functions, are considered as one of the most promising materials for catalysis, molecular adsorption separation, drug delivery and fluorescence sensing.[5–7] A representative study made by Lillerud's group reported a series of UiO-type ZrMOFs with excellent stability and large specific surface area.[8] Since then, research studies on the synthesis and properties of ZrMOFs have sprung up.[9–13] It is worth noting that Zhou and coworkers reported multifarious PCN-type ZrMOFs.[14] Intriguingly, they exploited heterometallic MOFs by cooperative cluster metalation and ligand migration and sequential transformation.[15] Recently, by virtue of using a trinuclear Zr_3-based metallo-pyridine ligand, Cui and coworkers achieved the highly specific coordination-driven construction of heterometallic ZrMOFs, where unprecedented nonanuclear Zroxocarboxylate clusters are first discovered.[16]

Taking the aforementioned prominent work into consideration, our strategy is to use a presynthesized trinuclear zirconocene-based precursor (Fig. 1c) as a zirconium source for the generation of heterometallic MOFs by combining with various transition metal cations. Consequently, two 2D heterometallic Zr-MOFs were obtained (Fig. 1d and S1†): $[Zr_6(C_5H_5)6O_2(INA)_6CoCl_4]\cdot 4DMA\cdot 5H_2O$ (denoted as ZrMOF-Co) and $[Zr_6(C_5H_5)6O_2(INA)_6NiCl_4]\cdot 4DMA\cdot 16H_2O$ (denoted as ZrMOF-Ni) (INA^- = the anion of isonicotinic acid), respectively. Solvent molecules are estimated by the combination of the SQUEEZE calculation results and thermogravimetric and elemental analyses.

The synthetic process for a trinuclear zirconocene-based metallo-pyridine precursor was slightly modified according to the literature,[16,17] and the details of the synthetic procedure are given in the ESI.† Single crystals of **ZrMOF-Co** and **ZrMOF-Ni** were successfully obtained by reacting the Zr_3 precursor and cobalt chloride hexahydrate or nickel nitrate hexahydrate in *N*,*N*-dimethylacetamide (DMA) at 70 °C for 12 h. It is noteworthy that we have tried to replace DMA with another frequently-used solvent, *N*,*N*-dimethylformamide (DMF), but no crystals were

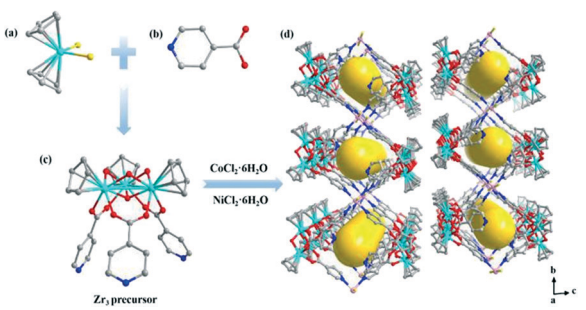

Fig. 1 (a) Cp_2ZrCl_2 (Cp = η_5-C_5H_5), (b) isonicotinic acid, and (c) the trinuclear zirconocene-based precursor. (d) The crystal structure of ZrMOF-Co or ZrMOF-Ni. Color code: Zr, turquoise; Cl, yellow; Co or Ni, light pink; O, red; N, blue; C, grey.

[a] *College of Chemical Engineering, Northeast Electric Power University, Jilin City 132012, PR China. E-mail: zhangyuteng@neepu.edu.cn*
[b] *School of Chemical and Pharmaceutical Engineering, Jilin Institute of Chemical Technology, Jilin, 132022, PR China. E-mail: lishb997@nenu.edu.cn*

† Electronic supplementary information (ESI) available: Crystallographic data in CIF format, PXRD, IR, and TGA data. CCDC 2109221 and 2109222 contain the supplementary crystallographic data for this paper. For ESI and crystallographic data in CIF or other electronic format see DOI: 10.1039/d1ce01418h

achieved. To some extent, it can be seen that the DMA solvent is more applicable to this reaction system.

The phase purities of ZrMOF-Co and ZrMOF-Ni are confirmed by the agreement between the experimental powder X-ray diffraction (PXRD) pattern and the simulated pattern generated from structural analysis (Fig. S3 and S4†). Single-crystal X-ray structural analyses reveal that the two compounds crystallize in the triclinic system with the space group $P\bar{1}$. They both maintain molecular building blocks (MBBs) consisting of Zr_3-oxycarboxylic acid ligands, which have a symmetry similar to C_{3v} with the carboxylate ligands orientated to one face and the μ_2-OH groups to the other (Fig. S2†). The average Zr–O–Zr angle is 104.38°. Each carboxylate linker is symmetrically connected with two adjacent Zr atoms (av. Zr–O(carboxylate) 2.204 Å). The central μ_3-O atom is equally coordinated to all three Zr centres (av. Zr–O_c 2.123 Å).

In view of the isomorphism of the two compounds, ZrMOF-Co is described as an example. For ZrMOF-Co, its asymmetric unit (Fig. 2a) contains a trinuclear zirconocene-based isonicotinic ligand, two DMA molecules, two Cl atoms and one Co atom. There are two types of Cl atoms, one of which is coordinated by a Co atom. Notably, the other Cl atom is dissociated, acting as a counteranion to balance the positive charge. The distance between this free Cl atom and the two adjacent Zr atoms ranges from 4.640 to 4.677 Å, as shown in Fig. 2b. Except for the two coordinated Cl atoms, four N atoms from four bridging INA ligands are connected with a Co atom, leading to an octahedral configuration of a Co centre (Fig. 2c). The bond length between the cobalt atom and the nitrogen atoms (from INA ligands) is in the range of 2.210–2.240 Å.

The IR spectra of the two compounds were investigated. The absorption band near 3300 cm^{-1} is due to the stretching vibration of the O–H bond. The peak at 1627 cm^{-1} is attributed to the N–H stretching vibration.[18] The sharp peak at 1542 cm^{-1} indicates the stretching vibrations of the C=C bond. The peak at 1261 cm^{-1} belongs to the C–N stretching absorption.[19] In addition, the absorption peak at 607 cm^{-1} is ascribed to the characteristic stretching vibration of the Zr–O bond.

To investigate the thermal stabilities of ZrMOF-Co and ZrMOF-Ni, TGA experiments for both compounds were carried out from room temperature to 800 °C under a nitrogen atmosphere. As seen from Fig. S6 and S7 in the ESI,† the two compounds exhibit weak thermal stability. For ZrMOF-Co, the first weight loss of 3.74% in the range 25–100 °C is comparable with the calculated value of 3.68%, due to the removal of 5 H_2O molecules. Subsequently, the second weight loss is 14.08% in the temperature range *ca.* 100–200 °C, which is attributed to the removal of 4 DMA molecules (calcd 14.24%). As the temperature continues to rise, the structure starts to collapse, and the final product is ZrO_2. ZrMOF-Ni exhibits a continuous weight loss of 24.32% from 25–190 °C, which is mainly attributed to the removal of 16 H_2O molecules (calcd 10.29%) and 4 DMA molecules (calcd 13.26%). As the temperature increases, the structure starts to collapse, leading to the formation of the final product ZrO_2.

The chemical state of the two ZrMOFs was analyzed by X-ray photoelectron spectroscopy (XPS) measurements. As shown in Fig. S8 and S9,† the presence of O, N, C, Zr, and Co or Ni in the two ZrMOFs was confirmed. The Co2p XPS spectrum (Fig. 3a) of ZrMOF-Co exhibits two major peaks at 781.1 and 797.1 eV, corresponding to $Co2p_{3/2}$ and $Co2p_{1/2}$, respectively, and the two weak bands at 785.8 and 802.7 eV are the $Co2p_{3/2}$ and $Co2p_{1/2}$ satellite signals, respectively. The spin-energy separation between the $Co2p_{3/2}$ peak and the $Co2p_{1/2}$ peak is approximately at 15.8 eV, which is characteristic of Co^{2+} as previously reported.[20,21] Fig. 3b

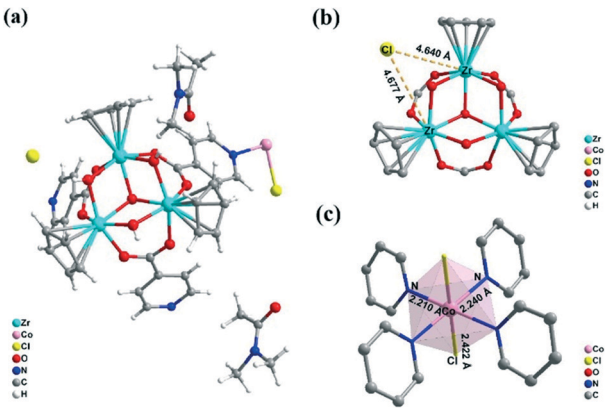

Fig. 2 (a) The asymmetric unit of ZrMOF-Co, (b) the coordination environment of the dissociative Cl atom, and (c) the octahedral Co atom.

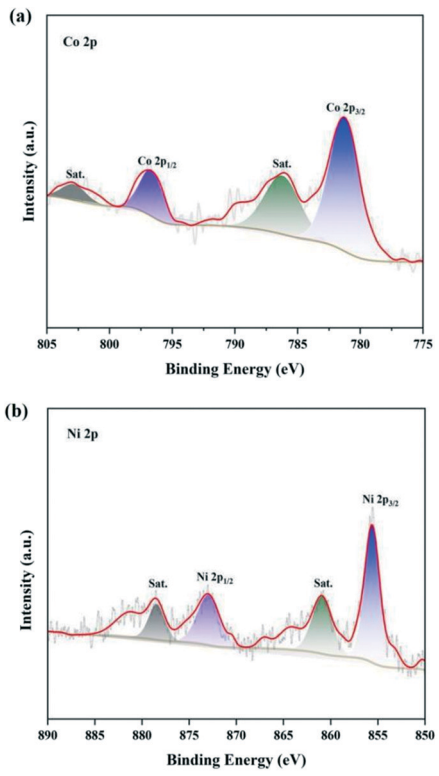

Fig. 3 (a) The Co2p XPS spectrum of ZrMOF-Co. (b) The Ni2p XPS spectrum of ZrMOF-Ni.

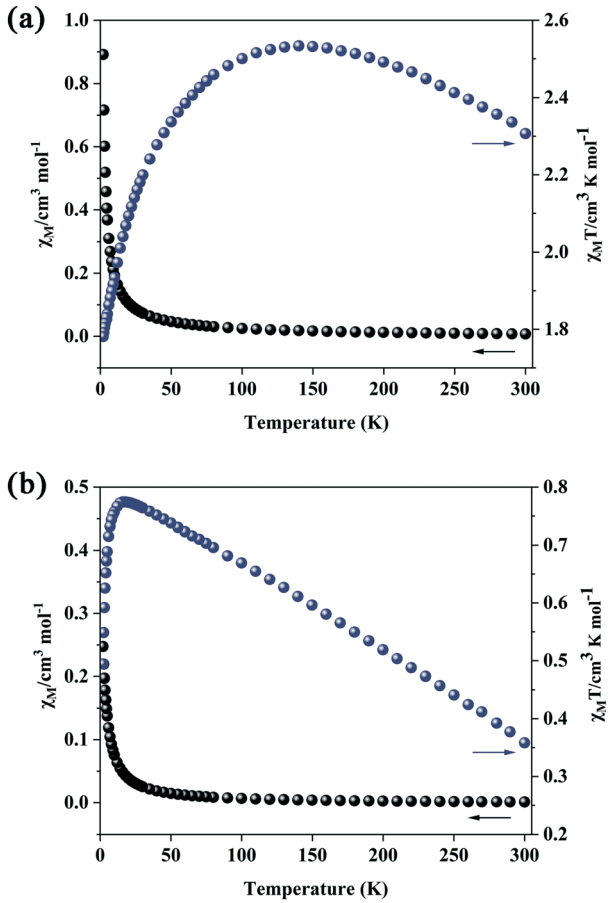

Fig. 4 Temperature dependence of χ_M and $\chi_M T$ of (a) ZrMOF-Co and (b) ZrMOF-Ni.

shows the XPS spectrum in the Ni2p region. Two strong peaks at 873.9 and 856.3 eV can be assigned to $Ni2p_{1/2}$ and $Ni2p_{3/2}$, respectively, associated with two satellite peaks at 862.1 and 880.5 eV,[22] implying the presence of Ni in the divalent state form.

The temperature-dependent magnetic susceptibilities of the two ZrMOFs were measured over the range of 2–300 K. The plots of the molar magnetic susceptibility χ_M and $\chi_M T$ *versus* T of ZrMOF-Co and ZrMOF-Ni under a constant magnetic field of 1000 Oe are shown in Fig. 4. As can be seen from Fig. 4a, the $\chi_M T$ value of ZrMOF-Co at 300 K is 2.30 cm^3 K mol^{-1}. It is slightly higher than the theoretical value of 1.875 cm^3 K mol^{-1} for an uncoupled high-spin Co(II) ion (S = 3/2, g = 2),[23] which is consistent with the orbital contribution of the divalent cobalt ion, mainly due to the stronger spin–orbit coupling in the Co(II) ion, which in turn leads to the occurrence of magnetic anisotropy in the Co(II) ion. Then, the $\chi_M T$ value slowly increases from 2.30 cm^3 K mol^{-1} to 2.53 cm^3 K mol^{-1}, the $\chi_M T$ value slowly decreases from 2.53 cm^3 K mol^{-1} to 2.42 cm^3 K mol^{-1} at 60 K, and upon cooling, the $\chi_M T$ value reaches a minimum of 1.78 cm^3 K mol^{-1}. The temperature dependence of the reciprocal susceptibilities (χ_M^{-1}) conforms to the Curie–Weiss law above 2 K with a negative Weiss constant of θ = −0.79 K and a Curie constant of C = 2.43 cm^3 K mol^{-1} (Fig. S10†), further supporting the presence of antiferromagnetic interactions in ZrMOF-Co. Besides, a magnetic behavior is observed for ZrMOF-Ni (Fig. 3b), and the $\chi_M T$ value of ZrMOF-Ni gradually increases from 0.35 cm^3 K mol^{-1} to 0.77 cm^3 K mol^{-1} at 14 K and then quickly decreases to 0.48 cm^3 K mol^{-1}. The thermal variation of the molar susceptibility obeys the Curie–Weiss law over the range 55–200 K. The values of the Weiss and Curie constants are θ= 24.84 K and C = 0.48 cm^3 K mol^{-1} (Fig. S11†). The positive θ value supports the presence of intermolecular ferromagnetic interactions in **ZrMOF-Ni**.[24,25]

Focusing on the potential applications of these ZrMOFs, the fabrication of nanostructured materials derived from the pyrolysis of MOFs has been confirmed as an effective route.[26,27] Heterometallic MOFs containing cobalt or nickel are commonly considered as potential candidate materials for the preparation of MOF derivatives.[28] Herein, ZrMOF-Co and ZrMOF-Ni may serve as sacrificial templates/precursors to prepare functional MOF derivatives with potential photo and electrochemical activities and durability for applications in electrochemical energy storage and catalysis.

In summary, two isostructural two-dimensional heterometallic ZrMOFs have been successfully synthesized by a stepwise synthesis strategy. Single-crystal X-ray structural analyses reveal that they are both constructed from a presynthesized Zr_3-based INA precursor, leading to a two-dimensional infinite chain structure. Furthermore, the magnetic studies indicate that ZrMOF-Co shows antiferromagnetic performance, while ZrMOF-Ni features a ferromagnetic behavior. The incorporated presynthesized Zr_3 carboxylate pyridine ligand not only adds a representative example to the limited family of Zr-based building blocks, but also will be regarded as an outstanding 3-connected linker which is potentially suited for constructing other Zr-based metal organic materials.

Author contributions

Juan Zhu: conceptualization, methodology, data curation, and writing – original draft. Zhao-Yang Liu: formal analysis and validation. Shuang-bao Li: formal analysis, resources, and writing – review & editing. He Huang: investigation. Bao-Xu Jiang: data curation. Yu-Teng Zhang: supervision, funding acquisition, project administration, and writing – review & editing.

Conflicts of interest

There are no conflicts to declare.

Acknowledgements

This work was financially supported by the National Natural Science Foundation of China (21901034), the Education Department of Jilin Province (JJKH20190692KJ), and the Youth Science and Technology Talent Promotion Project of Jilin Province (QT202023). The authors

acknowledge the assistance of JLICT Center of Characterization and Analysis.

Notes and references

1 J. Dong, Y. Liu and Y. Cui, *J. Am. Chem. Soc.*, 2020, **143**, 390–398.
2 M. Bazargan, F. Ghaemi, A. Amiri and M. Mirzaei, *Coord. Chem. Rev.*, 2021, **445**, 214107.
3 C. Wang, B. An and W. Lin, *ACS Catal.*, 2019, **9**, 130–146.
4 J. Liu, S. Mukherjee, F. Wang, R. A. Fischer and J. Zhang, *Chem. Soc. Rev.*, 2021, **50**, 5706–5745.
5 X. Song, D. Hu, X. Yang, H. Zhang, W. Zhang, J. Li, M. Jia and J. Yu, *ACS Sustainable Chem. Eng.*, 2019, **7**, 3624–3631.
6 J. Gu, X. Sun, L. Kan, J. Qiao, G. Li and Y. Liu, *ACS Appl. Mater. Interfaces*, 2021, **13**, 41680–41687.
7 X. Zheng, Y. Zhao, P. Jia, Q. Wang, Y. Liu, T. Bu, M. Zhang, F. Bai and L. Wang, *Inorg. Chem.*, 2020, **59**, 18205–18213.
8 J. Cavka, S. Jakobsen, U. Olsbye, N. Guillou, C. Lamberti, S. Bordiga and K. Lillerud, *J. Am. Chem. Soc.*, 2008, **130**, 13850–13851.
9 C. Chen, Z. Wei, J. Jiang, Y. Fan, S. Zheng, C. Cao, Y. Li, D. Fenske and C. Su, *Angew. Chem.*, 2016, **128**, 10086–10090.
10 X. Yang, S. Yuan, L. Zou, H. Drake, Y. Zhang, J. Qin, A. Alsalme and H. Zhou, *Angew. Chem.*, 2018, **130**, 3991–3996.
11 A. Cadiau, L. Xie, N. Kolobov, A. Shkurenko, M. Qureshi, M. Tchalala, S. Park, A. Bavykina, M. Eddaoudi, M. Dincă, C. Hendon and J. Gascon, *Chem. Mater.*, 2020, **32**, 97–104.
12 C. Fu, H. Zhou, L. Tan, Z. Huang, Q. Wu, X. Ren, J. Ren and X. Meng, *ACS Nano*, 2018, **12**, 2201–2210.
13 S. Luo, Z. Zeng, G. Zeng, Z. Liu, R. Xiao, M. Chen, L. Tang, W. Tang, C. Lai, M. Cheng, B. Shao, Q. Liang, H. Wang and D. Jiang, *ACS Appl. Mater. Interfaces*, 2019, **11**, 32579–32598.
14 S. Yuan, J. Qin, J. Su, B. Li, J. Li, W. Chen, H. Drake, P. Zhang, D. Yuan, J. Zuo and H. Zhou, *Angew. Chem., Int. Ed.*, 2018, **57**, 12578–12583.
15 M. Bosch, S. Yuan, W. Rutledge and H. Zhou, *Acc. Chem. Res.*, 2017, **50**, 857–865.
16 W. Gong, H. Arman, Z. Chen, Y. Xie, F. Son, H. Cui, X. Chen, Y. Shi, Y. Liu, B. Chen, O. Farha and Y. Cui, *J. Am. Chem. Soc.*, 2021, **143**, 657–663.
17 M. Maity, P. Howlader and S. Mukherjee, *Cryst. Growth Des.*, 2018, **18**, 6956–6964.
18 L. Shen, S. Liang, W. Wu, R. Liang and L. Wu, *Dalton Trans.*, 2013, **42**, 13649–13657.
19 M. Sarker, J.-Y. Song and S.-H. Jhung, *Chem. Eng. J.*, 2018, **331**, 124–131.
20 Z. Wang, C. Gao, Y. Liu, D. Li, W. Chen, Y. Ma and C. Wang, *Mater. Lett.*, 2017, **193**, 216–219.
21 T. Xue and J. Lee, *J. Power Sources*, 2014, **245**, 194–202.
22 Q. Liu, L. Xie, X. Shi, G. Du, A. Asiri, Y. Luo and X. Sun, *Inorg. Chem. Front.*, 2018, **5**, 1570–1574.
23 F. Lloret, M. Julve, J. Cano, R. García and E. Pardo, *Inorg. Chim. Acta*, 2008, **361**, 3432–3445.
24 G. An, H. Wang, A. Cui and H. Kou, *New J. Chem.*, 2014, **38**, 5037–5042.
25 J. Li, Z. Du, L. Xiong, L. Fu and W. Bo, *J. Solid State Chem.*, 2021, **293**, 121799.
26 J.-K. Sun and Q. Xu, *Energy Environ. Sci.*, 2014, **7**, 2071–2100.
27 W. Xia, A. Mahmood, R. Zou and Q. Xu, *Energy Environ. Sci.*, 2015, **8**, 1837–1866.
28 D. Meng, Q. Li, Y. Zhao, C. Liu and H. Pang, *Coord. Chem. Rev.*, 2020, **416**, 213341.

